JYX JYVÄSKYLÄN YLIOPISTO UNIVERSITY OF JYVÄSKYLÄ

This is a self-archived version of an original article. This version may differ from the original in pagination and typographic details.

Author(s): Osadchuk, Irina; Konrad, Nele; Truong, Khai-Nghi; Rissanen, Kari; Clot, Eric; Aav, Riina; Kananovich, Dzmitry; Borovkov, Victor

Title: Supramolecular Chirogenesis in Bis-Porphyrin : Crystallographic Structure and CD Spectra for a Complex with a Chiral Guanidine Derivative

Year: 2021

Version: Published version

Copyright: © 2021 by the authors. Licensee MDPI, Basel, Switzerland

Rights: CC BY 4.0

Rights url: https://creativecommons.org/licenses/by/4.0/

Please cite the original version:

Osadchuk, I., Konrad, N., Truong, K.-N., Rissanen, K., Clot, E., Aav, R., Kananovich, D., & Borovkov, V. (2021). Supramolecular Chirogenesis in Bis-Porphyrin : Crystallographic Structure and CD Spectra for a Complex with a Chiral Guanidine Derivative. Symmetry, 13(2), Article 275. https://doi.org/10.3390/sym13020275

symmetry

MDPI

Article

Supramolecular Chirogenesis in Bis-Porphyrin: Crystallographic Structure and CD Spectra for a Complex with a Chiral Guanidine Derivative

Irina Osadchuk [1,2], Nele Konrad [1], Khai-Nghi Truong [3], Kari Rissanen [3], Eric Clot [2], Riina Aav [1], Dzmitry Kananovich [1,*] and Victor Borovkov [1,*]

[1] School of Science, Department of Chemistry and Biotechnology, Tallinn University of Technology, Akadeemia tee 15, 12618 Tallinn, Estonia; irina.osadchuk@taltech.ee (I.O.); nele.konrad@taltech.ee (N.K.); riina.aav@taltech.ee (R.A.)
[2] ICGM, University Montpellier, CNRS, ENSCM, 34000 Montpellier, France; eric.clot@umontpellier.fr
[3] Department of Chemistry, University of Jyväskylä, P.O. Box 35, Survontie 9B, 40014 Jyväskylä, Finland; khai-nghi.kn.truong@jyu.fi (K.-N.T.); kari.t.rissanen@jyu.fi (K.R.)
* Correspondence: dzmitry.kananovich@taltech.ee (D.K.); victor.borovkov@taltech.ee (V.B.)

Abstract: The complexation of (3a*R*,7a*R*)-*N*-(3,5-bis(trifluoromethyl)phenyl)octahydro-2*H*-benzo[*d*]imidazol-2-imine (BTI), as a guest, to ethane-bridged bis(zinc octaethylporphyrin), bis(ZnOEP), as a host, has been studied by means of ultraviolet-visible (UV-Vis) and circular dichroism (CD) absorption spectroscopies, single crystal X-ray diffraction, and computational simulation. The formation of 1:2 host-guest complex was established by X-ray diffraction and UV-Vis titration studies. Two guest BTI molecules are located at the opposite sides of two porphyrin subunits of bis(ZnOEP) host, which is resting in the *anti*-conformation. The complexation of BTI molecules proceed via coordination of the imine nitrogens to the zinc ions of each porphyrin subunit of the host. Such supramolecular organization of the complex results in a screw arrangement of the two porphyrin subunits, inducing a strong CD signal in the Soret (B) band region. The corresponding DFT computational studies are in a good agreement with the experimental results and prove the presence of 1:2 host-guest complex as the major component in the solution (97.7%), but its optimized geometry differs from that observed in the solid-state. The UV-Vis and CD spectra simulated by using the solution-state geometry and the TD-DFT/ωB97X-D/cc-pVDZ + SMD (CH2Cl2) level of theory reproduced the experimentally obtained UV-Vis and CD spectra and confirmed the difference between the solid-state and solution structures. Moreover, it was shown that CD spectrum is very sensitive to the spatial arrangement of porphyrin subunits.

Keywords: porphyrin; guanidine; host–guest binding; chirality; supramolecular chemistry; circular dichroism; DFT; TD-DFT simulation

check for updates

Citation: Osadchuk, I.; Konrad, N.; Truong, K.-N.; Rissanen, K.; Clot, E.; Aav, R.; Kananovich, D.; Borovkov, V. Supramolecular Chirogenesis in Bis-Porphyrin: Crystallographic Structure and CD Spectra for a Complex with a Chiral Guanidine Derivative. *Symmetry* **2021**, *13*, 275. https://doi.org/10.3390/sym13020275

Academic Editor: Rui Tamura
Received: 15 January 2021
Accepted: 1 February 2021
Published: 5 February 2021

Publisher's Note: MDPI stays neutral with regard to jurisdictional claims in published maps and institutional affiliations.

Copyright: © 2021 by the authors. Licensee MDPI, Basel, Switzerland. This article is an open access article distributed under the terms and conditions of the Creative Commons Attribution (CC BY) license (https://creativecommons.org/licenses/by/4.0/).

1. Introduction

Porphyrins play an important role in different fields of science and technology, including catalysis [1–3], light harvesting [4–6], medicine [7–10], supramolecular systems [11–21], electronic devices [16–18], etc. Besides, porphyrin-based systems have found broad application as chemical and chirality sensors [19–22] because of their notable property to form supramolecular assemblies with different guest molecules. These assemblies produce characteristic absorption bands in the low-energy regions of the corresponding UV-Vis and circular dichroism (CD) spectra, which are essentially shifted from absorption of the majority of analytes [23–26]. Recently, much attention has also been paid to the phenomena of supramolecular chirogenesis, where a chiral guest determines the supramolecular chirality of the entire host-guest system upon binding to an achiral host molecule [12–15,20,23–35]. In the case of ethane-bridged bis(zinc porphyrin)s (bis(ZnOEP)s) (Figure 1), steric hindrance induced by coordination of a chiral guest forces the supramolecular system to adopt a screw

conformation, with the chirality of a guest determining either a clockwise or anticlockwise arrangement of porphyrin units in the bis-porphyrin host [30–32]. In turn, this directional helicity results in induced CD in the porphyrin absorption region due to exciton coupling between the corresponding electronic transitions. This phenomenon has been successfully applied for determination of the absolute configuration of various chiral organic compounds, including amines [27,29,33], amino acid derivatives [33], alcohols [15], carboxylic acids [15], and epoxides [34]. For the zinc porphyrin-based sensing systems, amines and other basic nitrogen-containing organic compounds are particularly privileged analytes due to their strong electrostatic (Lewis acid-base) binding to zinc ion, which produces the corresponding penta-coordinated zinc porphyrin complexes in general [31,32,35].

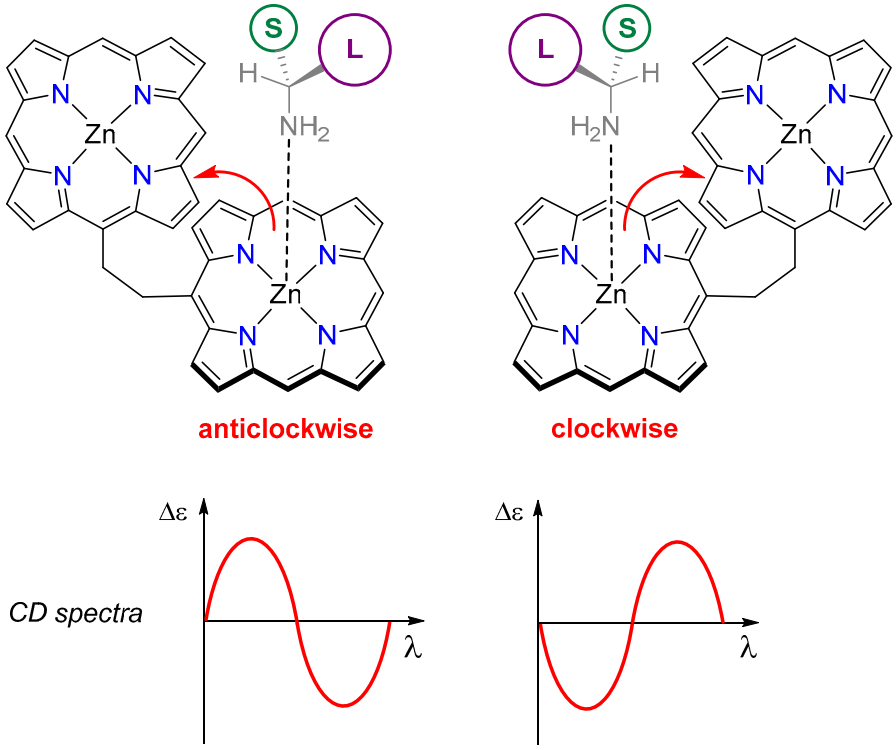

Figure 1. Schematic representation of complexes of bis(ZnOEP) with both enantiomers of a chiral amine and the corresponding CD signal induction. Ethyl substituents in bis(ZnOEP) are omitted for clarity. "S" and "L" denotes small and large substituents in a chiral amine guest, respectively. See [30–32] for the experimental CD spectra.

As a part of our ongoing studies towards application of bis(ZnOEP) for sensing polyfunctionalized chiral organic molecules, here we report the complexation of a chiral guanidine compound, (3a*R*,7a*R*)-*N*-(3,5-bis(trifluoromethyl)phenyl)octahydro-2*H*-benzo[*d*]imidazol-2-imine (BTI, Figure 2), with bis(ZnOEP) [36]. Complexation and supramolecular chirogenesis phenomena in the selected host-guest system were studied by means of UV-Vis, CD spectroscopies, and single crystal X-ray analysis. The experimental results were fully rationalized with the aid of computational simulation. Special attention was paid to the reasons why experimental CD spectra in many cases are different from the simulated, especially in the case of chiral porphyrin-based supramolecular systems with a certain degree of conformational flexibility.

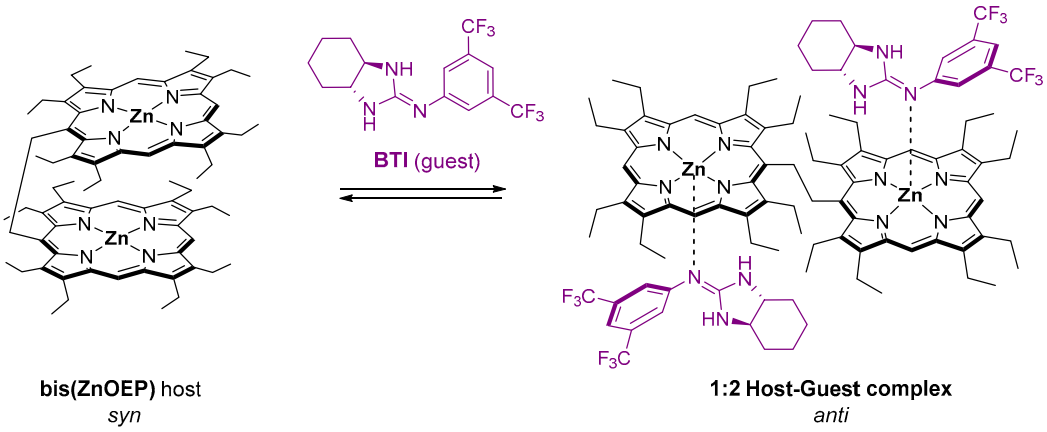

Figure 2. Complexation between bis(ZnOEP) (host) in *syn* conformation and BTI (guest) resulting in *anti*-conformation of the 1:2 host-guest complex in CH_2Cl_2 solution.

2. Materials and Methods

General methods. UV-Vis absorption spectra were recorded on a Jasco V-730 double-beam spectrophotometer in a 1-cm thermally stabilized screw-cap quartz cuvette with a septum cap. CD spectrum were recorded on a Jasco J-1500 spectrophotometer in a 1-cm screw cap quartz cuvette in analytical-grade CH_2Cl_2 at 20 °C. Data acquisition was performed in the 375–475-nm range with a scanning rate of 50 nm/min, bandwidth of 2.6 nm, response time of 4 s, and accumulations in 3 scans. ^{1}H NMR spectra of BTI were recorded on a Bruker Avance III 400 MHz spectrometer. The chemical shifts (δ) are reported in ppm and referenced to a $CHCl_3$ residual peak at 7.26 ppm for ^{1}H NMR, and a $CDCl_3$ peak at 77.16 ppm for ^{13}C NMR. HRMS measurement for BTI was performed on an Agilent 6540 UHD Accurate-Mass Q-TOF LC/MS system (Agilent Technologies, Santa Clara, CA, USA) equipped with an AJS-ESI source.

Materials. Bis(ZnOEP) was prepared as described in [36]. BTI was prepared by intramolecular cyclization of 1-((1*R*,2*R*)-2-aminocyclohexyl)-3-(3,5-bis(trifluoromethyl)phenyl)thiourea [37] following the experimental procedure described in [38].

(3a*R*,7a*R*)-*N*-(3,5-bis(trifluoromethyl)phenyl)octahydro-2*H*-benzo[*d*]imidazol-2-imine (BTI): ^{1}H NMR (400 MHz, $CDCl_3$) δ = 7.43 (s, 1H), 7.39 (s, 2H), 5.20 (br s, 2H, NH), 3.17–3.04 (m, 2H), 2.01–1.89 (m, 2H), 1.89–1.73 (m, 2H), 1.54–1.21 (m, 4H). ^{13}C NMR (100.6 MHz, $CDCl_3$) δ = 159.0, 151.4, 132.5 (q, J_{CF} = 32.9 Hz), 123.6 (q, J_{CF} = 272.9 Hz, CF_3), 123.2, 115.2 (m, J_{CF} = 4.1 Hz), 61.8, 29.6, 24.0. HRMS (ESI) *m*/*z* calcd for $C_{15}H_{16}F_6N_3^+$ $[M + H]^+$ 352.1243, found 352.1252.

Spectroscopic Titrations. All the solutions were prepared and mixed by using properly calibrated analytic glassware (Hamilton® Gastight syringes, volumetric flasks). All weights were balanced with a Radwag MYA 11.4 microbalance (accuracy ± 6 μg). The concentration of zinc porphyrin was held constant throughout the titration sequence. The titration data were fitted globally by using online software Bindfit [39–41]. UV-Vis spectrophotometric titration experiments were performed in analytical-grade CH_2Cl_2. To a solution of zinc porphyrin, a solution of guest (dissolved in a stock solution of the host to keep the concentration of the host constant) was added portion-wise using a gastight syringe at 20 °C. The changes in the bathochromic shift of the Soret band were monitored at different concentrations of the guest.

Single crystal X-ray analysis. The data was measured using a dual-source Rigaku SuperNova diffractometer equipped with an Atlas detector and an Oxford Cryostream cooling system using mirror-monochromated Mo-K_α radiation (λ = 0.71073 Å). Data collection and reduction for all complexes were performed using the program CrysAlisPro [42] and the Gaussian face-index absorption correction method was applied [42]. All structures were solved with Direct Methods (*SHELXS*) [43–45] and refined by full-matrix least squares based on F^2 using *SHELXL*-2013 [43–45]. Non-hydrogen atoms were assigned anisotropic

displacement parameters unless stated otherwise. Hydrogen atoms were placed in idealized positions and included as riding. Isotropic displacement parameters for all H atoms were constrained to multiples of the equivalent displacement parameters of their parent atoms with $U_{iso}(H) = 1.2\ U_{eq}$ (parent atom). Enhanced rigid bond restraints (RIGU) [46,47] with standard uncertainties of 0.001 $Å^2$ were applied for several atom pairs as well as distance restraints (DFIX). Positional disorder of the trifluoromethyl (CF_3) groups is observed. Split positions were assigned with isotropic displacement parameters: site occupancy refinement converged to 54.2(6)% to 45.8(6)% with the sum of the site occupancies of both alternative positions constrained to unity. The X-ray single crystal data, experimental details, and CCDC number (2051302) are given below.

Crystal data for the 1:2 complex of bis(ZnOEP) and BTI: CCDC-2051302, $C_{104}H_{120}F_{12}N_{14}Zn_2$, M = 1924.87 $gmol^{-1}$, purple plate, 0.10 × 0.08 × 0.03 mm^3, triclinic, space group *P*1 (No. 1), a = 10.2054(4) Å, b = 13.0749(6) Å, c = 18.7677(8) Å, α = 82.751(4)°, β = 79.844(3)°, γ = 77.298(4)°, V = 2394.71(18) $Å^3$, Z = 1, D_{calc} = 1.335 gcm^{-3}, F(000) = 1010, μ = 1.270 mm^{-1}, T = 120(2) K, θ_{max} = 76.019°, 14,864 total reflections, 8633 with $I_o > 2\sigma(I_o)$, R_{int} = 0.0431, 10,559 data, 1194 parameters, 61 restraints, GooF = 1.029, R_1 = 0.0600 and wR_2 = 0.1417 [$I_o > 2\sigma(I_o)$], R_1 = 0.0767 and wR_2 = 0.1544 (all reflections), $0.956 < d\Delta\rho < -0.668$ $eÅ^{-3}$.

Computational details. Structural optimization was performed using resolution of identity (RI) approximation [48–50], PB86 functional [51,52] with D3 dispersion correction [53] and def2-SV(P) basis set [54] implemented in Turbomole 7.0 [55], which showed good agreement with experimental data [56–58], as in a gas phase and in solvent. To include solvent effect the COSMO solvent model [59] was used. To confirm that the optimized geometry corresponds to a local minimum, the respective vibrational frequencies were calculated using the same program and level of theory. To get a more accurate energy value for Gibbs free energies calculations, a single point calculation was done using the RI-BP86/def2-TZVP [60] level of theory and COSMO solvent model (ε = 8.93). The optimized geometries of supramolecular host-guest complexes are given in Geometries.xyz (provided in the Supplementary Materials).

The UV-Vis and CD spectra were simulated using the Gaussian16 [61] software and TD-DFT method [62–64]. For spectra simulations, the ωB97X-D functional [65] and cc-pVDZ basis set [66–68] with the SMD solvent model [69] were used, since this level of theory showed good agreement with experimental data [56,57,70]. The first 10 excited states were calculated in order to ensure that the B band region of the spectrum was covered. The corresponding data are given in the Supplementary Materials.

The UV-Vis and CD spectra and host-guest geometries were visualized using GaussView 6.0.16 [71]. For plotting the simulated spectra, a bandwidth of 0.04 eV was used due to its best agreement with the experimental spectra. The rotatory strengths were calculated on the basis of dipole velocity formalism.

3. Results

3.1. Absorption UV-Vis and CD Spectroscopy

As reported before, bis(ZnOEP) adopts a *syn*-conformation (Figure 3) in non-coordinating solvents (e.g., CH_2Cl_2) because of strong intramolecular π–π interactions between two porphyrin subunits [72]. Complexation with an external ligand results in the conformational switch to the corresponding *anti* form, which also causes dramatic changes in the UV-Vis spectra [31]. Similar to previously studied amine ligands [30–32], a portion-wise addition of BTI (Figure 3) resulted in a noticeable bathochromic shift of the Soret band and its split into two distinct absorption peaks at 426 and 437 nm that clearly indicates the formation of 1:2 host-guest complex with bis(ZnOEP) resting in the *anti*-conformation (Figure 2). As additional evidence, a Q(1,0) band at 559 nm was noticeably enhanced in comparison to the ligand free bis(ZnOEP) [31]. The resultant UV-Vis spectrum obtained at the final point of spectroscopic titration is shown on Figure 4A and consists of the following well-resolved absorption peaks, λ_{max}, nm (log ε): 426 (5.46), 437 (5.47), 561 (4.49), and 597 (4.00). Curve fitting of the absorbance change observed during the spectroscopic titration with

the 1:2 binding isotherm [39] yielded two association constants $K_1 = (0.51 \pm 0.01)\cdot 10^3$ M^{-1}, $K_2 = (3.1 \pm 0.1)\cdot 10^3$ M^{-1} at 293 K for the first and the second ligation events, respectively (Figure 3, Figures S1–S3 and Table S1, see the Supplementary Materials). More than a 6-fold increase of the second association constant is indicative of a highly positive cooperativity of the complexation process as it was found previously for other amine guests [73].

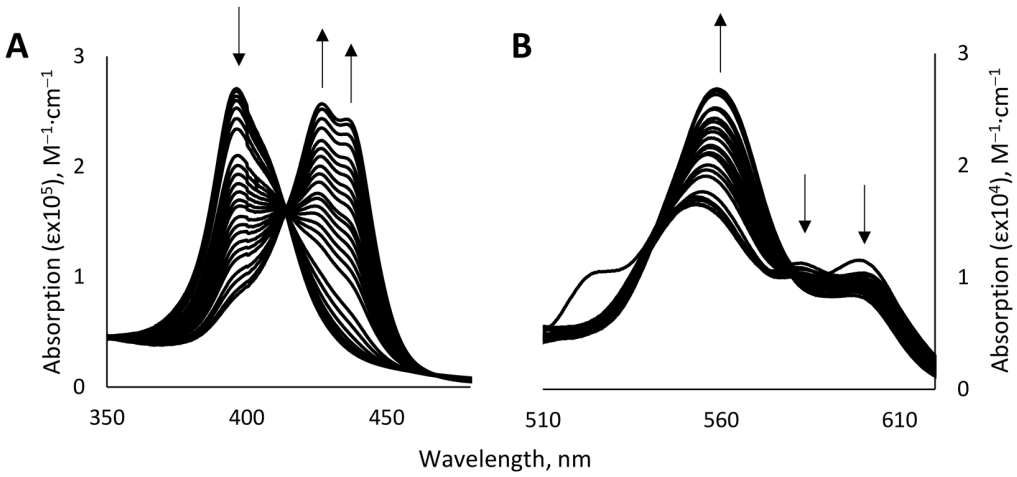

Figure 3. Changes in UV-Vis spectrum of bis(ZnOEP) ($3.34\cdot 10^{-6}$ M, CH_2Cl_2, 293 K) caused by portion-wise addition of BTI (0–1.79×10^{-3} M). (**A**) Soret-Bands region (**B**) Q-Bands region.

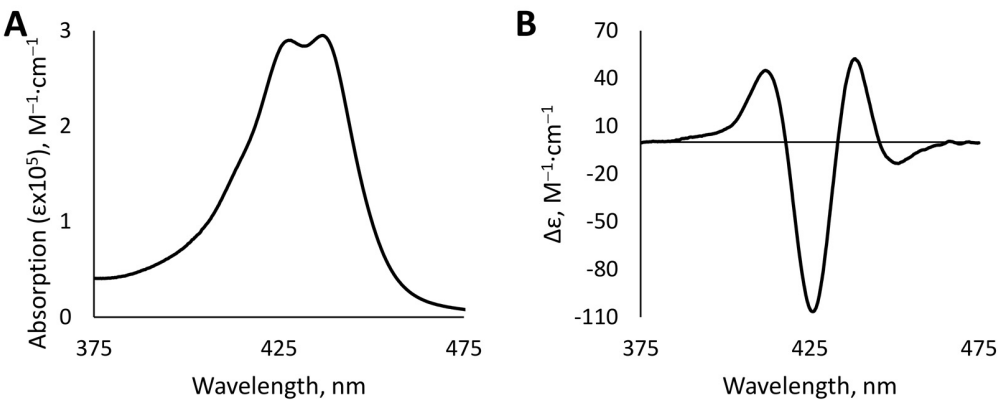

Figure 4. Experimental UV-Vis (**A**) and CD (**B**) spectra of 1:2 complex generated by mixing bis(ZnOEP) (3.34×10^{-6} M, CH_2Cl_2, 293 K) and BTI (4.41×10^{-3} M).

The CD spectrum of the resulting 1:2 host-guest complex (Figure 4B) was measured in CH_2Cl_2 at the end point of UV-Vis titration, after addition of the 1300-fold excess of BTI. This corresponds to 97% conversion of free bis(ZnOEP) host into the corresponding complex, and was calculated based on the values of the corresponding association constants and initial concentrations of the host and guest. While the parent bis-porphyrin is achiral and thus being CD silent, addition of BTI ligand induced a strong optical activity in the Soret transition region (Figure 4B). The observed CD profile consists of four Cotton effects (CEs): two positive peaks at 412 and 438 nm (with the intensities of 45 and 52 $M^{-1}\cdot cm^{-1}$, correspondingly), and two negative peaks at 426 and 451 nm (with the intensities of −106.5 and −13.5 $M^{-1}\cdot cm^{-1}$, correspondingly). Surprisingly, such a complicated CD profile is contrastingly distinguishable from more simple CD spectra of bis(ZnOEP) induced by conventional chiral amines [30–32]. Apparently, this is a result of the more complex structure of BTI in comparison to monodentate guests. To understand the origin of the observed chirogenic phenomenon, the corresponding computational studies were undertaken (see Section 3.3).

3.2. Single Crystal X-ray Structure

Crystallographic data provided an additional proof of the structure of 1:2 complex between bis(ZnOEP) and BTI, resting in the *anti*-conformation in the solid-state (Figure 5). Complexation proceeds via coordination of the imine nitrogen of BTI ligands to the zinc ions of bis(ZnOEP), with an average Zn–N bond distance of 2.18 Å. Commonly to zinc porphyrin complexes, zinc is penta-coordinated and slightly shifted out of the mean porphyrin plane towards the imine nitrogen of BTI ligand. Coordination of two guest molecules occurs from the opposite sides of bis(ZnOEP). In the solid-state, two porphyrin units are arranged nearly parallel to each other, with the Zn-C_{meso}-C_{meso}-Zn dihedral angle of 179.0°, hence indicating only a slight anticlockwise turn of the porphyrin moieties.

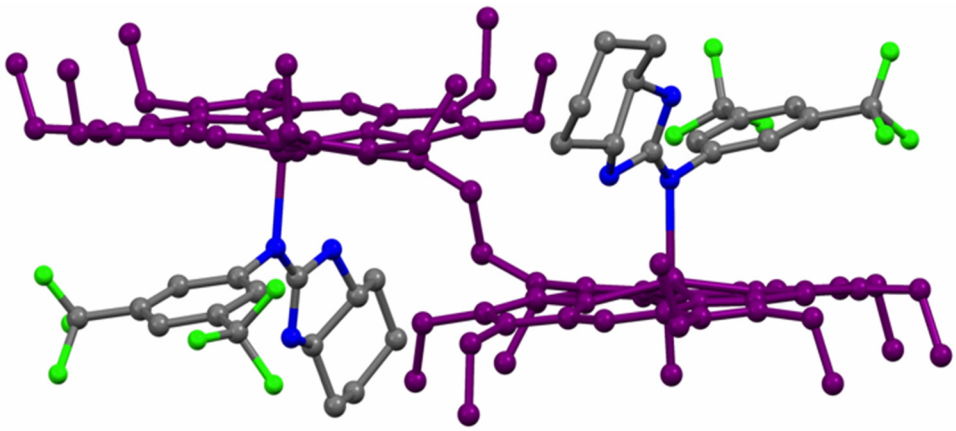

Figure 5. Ball-and-stick model of BTI-bis(ZnOEP) 2:1 complex according to X-ray studies (CCDC 2051302). Hydrogen atoms as well as atom sites with minor occupancies are omitted for clarity.

3.3. DFT Modelling of the Complex

The obtained crystal structure was used as a starting point for further geometry optimization. Three standard protocols were used as follows: (1) refining only the positions of hydrogens and fluorine atoms [74,75], (2) full optimization in the gas phase [74,76–78], and (3) full optimization in dichloromethane (COSMO solvent model) [76,77,79,80]. Optimization was performed using the RI-PB86-3D/def2-SV(P) level of theory followed by further simulation of the UV-Vis and CD spectra by using the ωB97X-D/cc-pVDZ level of theory with the SMD solvent model (see Figure 6 and Table S2 in the Supplementary Materials).

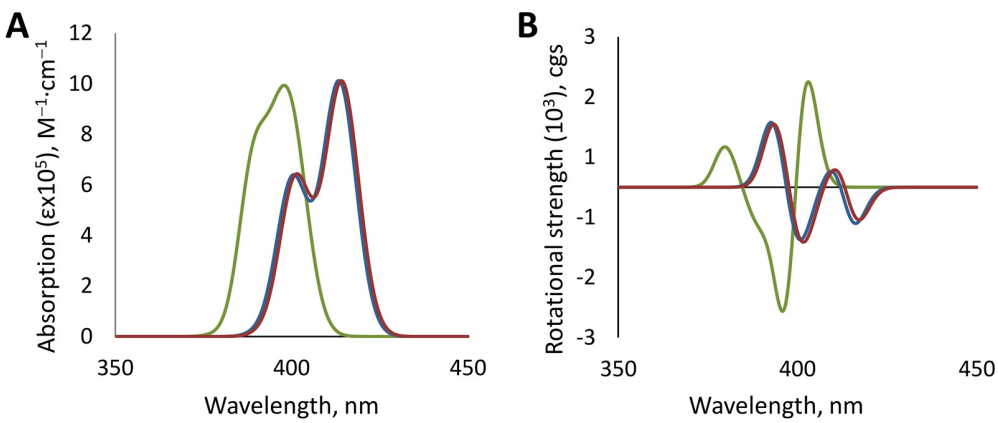

Figure 6. Simulated UV-Vis (**A**) and CD (**B**) spectra for the host-guest system, calculated by using different starting geometries and the ωB97X-D/cc-pVDZ and SMD solvent model. Green line—calculated based on crystal structure; blue line—calculated based on the structure optimized in the gas phase; red line—calculated based on optimized solution structure.

The UV-Vis spectra calculated on the basis of the crystal structure (λ_{max} at 391 and 399 nm) and optimized geometries (λ_{max} at 401 and 415 nm) are blue shifted in comparison to the experimentally obtained spectrum (λ_{max} at 426 and 437 nm) (Figure 6A). Additionally, it is of note that the absorption profile of the crystal structure-based spectrum shows a non-resolved split of the Soret band with only a shoulder at 391 nm due to the close proximity of the simulated electronic transitions. However, the optimized geometries in both the gas phase and the solution give nearly the same absorption profile with a well-resolved split Soret band, which is similar to the experimental spectrum.

In CD spectra, which are more sensitive to any geometry changes, the spectrum simulated using the crystal structure has three CEs: a positive peak of +670.0 cgs at λ_{max} at 380 nm, a negative peak of –2062.2 cgs at λ_{max} at 396 nm, and a positive peak of +1752.3 cgs at λ_{max} at 403 nm (Figure 6B). This spectrum is somewhat similar to the experimental one (Figure 4B), except the difference in the intensities of the positive bands and an absence of the low-energy negative band at 451 nm. As in the case of UV-Vis spectra, the CD spectral profiles simulated by using the geometries optimized in the gas phase and in dichloromethane solution are essentially the same (Figure 6B). Both spectra have four CEs: two positive peaks at 393 (393) and 490 (410) nm and two negative peaks at 409 (402) and 416 (417) nm in a gas phase and in dichloromethane (in brackets). However, the calculated intensities and shape of the bands are different from the experimental one.

To explain the differences in the calculated and experimental spectra, we assumed that the experimental spectrum represents the combined contribution of various conformers or even differently organized host-guest complexes. We attempted to define these species, since X-ray analysis usually defines only the most energetically favorable conformer. In addition to the lowest energy conformer **A** (which also dominates in the solid-state, according to X-ray analysis), three 1:2 complexes (**B**–**D**) differing by the spatial orientation of the guest molecules and two 1:1 complexes differing by the coordination mode to the second porphyrin moiety were built and their geometries were fully optimized. The calculated Gibbs free energies of these complexes are presented in Figure 7. In the complex **B**, two BTI molecules are placed asymmetrically at the opposite sides of the bis(ZnOEP) host. In the complexes **C** and **D**, the guests are located at the same side of bis(ZnOEP); however, both BTI molecules are facing each other either by the octahydrobenzo[d]imidazole fragments (complex **C**) or by the bis(trifluoromethyl)phenyl fragments (complex **D**). In addition to 1:2 complexes, two possible 1:1 complexes with clockwise and anticlockwise positions of two porphyrin subunits were also modelled. In the 1:1 complexes **E** and **F**, the host–guest interaction occurs via a two-point coordination mode in a tweezer fashion by placing the BTI molecule between two porphyrin moieties. As the most plausible binding modes, the corresponding tweezer conformation is fixed either by simultaneous coordination of two nitrogens of BTI with two zinc ions of bis(ZnOEP) (complex **E**) or by interaction of imino nitrogen and one fluorine atom of the CF_3 group with zinc ions of bis(ZnOEP) (complex **F**, Figure 7). All of the corresponding energies and geometries are given in Table S3 and Geometries.xyz (see the Supplementary Materials).

According to the Boltzmann distribution, the lowest energy complex **A** is a dominant species in solution (97.7%), whilst another complex **B** makes up only 1%, with the Gibbs free energy being by 2.8 kcal mol^{-1} higher than that of the complex **A**. The Gibbs free energies of the complexes **C** and **D** are even higher by 4.5 and 22.7 kcal mol^{-1}, which is quite reasonable considering the fact that the approach of two BTI molecules from the same side of bis(ZnOEP) is sterically hindered by the porphyrin's ethyl peripheral substituents. Formation of the 1:1 complexes **E** and **F** is also unfavorable, since their Gibbs free energies are 2.5 and 11.0 kcal mol^{-1} higher as compared to the major complex A. Based on these data, it is obvious that the formation of other complexes could not be the reason why the simulated spectra differ from the experimental one.

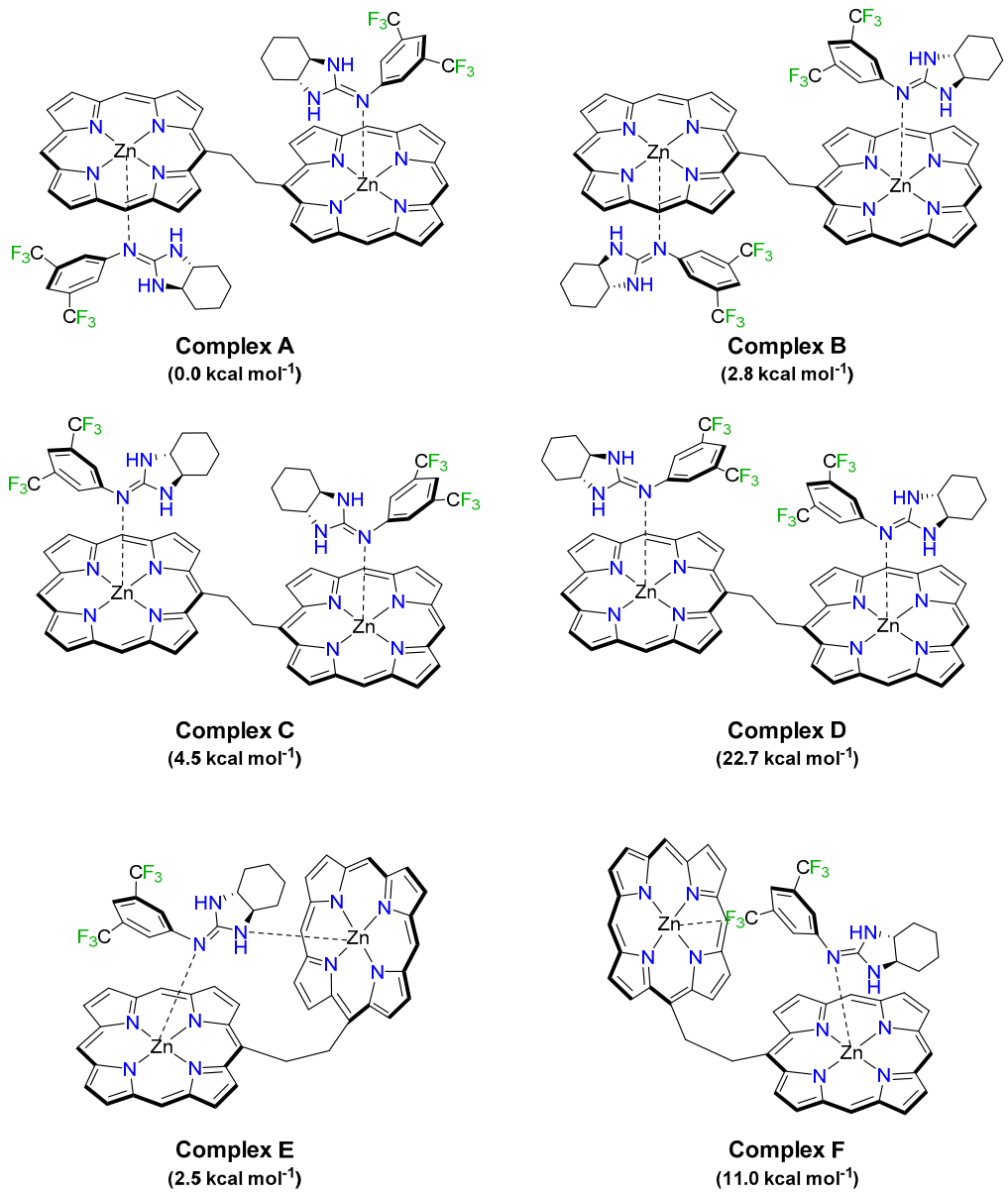

Figure 7. Plausible complexations modes (ratio 1:2 and 1:1) between bis(ZnOEP) and BTI and the corresponding relative Gibbs energies of the complexes in comparison with the lowest energy complex A. Ethyl substituents in bis(ZnOEP) are omitted for clarity.

In order to understand the differences with the experimental data, porphyrin geometries obtained from the crystal structure and optimized in solvent were compared and two major distinctions were found. In particular, one of the porphyrin planes is more deformed, with the C_β-C_β-$C_{\beta opp}$-$C_{\beta opp}$ dihedral angles being 18.1° and −15.2° (optimization in solution) and 9.4° and −9.3° (crystal structure), and porphyrin planes are shifted in respect to each other by 17.0° (based upon the Zn-C_{meso}-C_{meso}-Zn dihedral angle), as compared to the crystal structure geometry (Figure 8A and Table 1). Additionally, it turned out that solvation plays an insignificant role, resulting in the minor conformational changes found for the complexes optimized as in the gas phase and in CH_2Cl_2. For example, in the complex optimized in a gas phase, the Zn atoms became a bit closer to the average porphyrin planes (N-Zn-N_{opp} angle), but the C_β-C_β-$C_{\beta opp}$-$C_{\beta opp}$ and Zn-C_{meso}-C_{meso}-Zn dihedral angles remained almost unchanged. Therefore, it was reasonable to conclude that the differences observed between CD spectra, calculated using the geometries optimized in solution, and the crystal structure are attributed to altering the spatial position of the

two porphyrin units. Indeed, it is known that the CD spectra of bis-porphyrins are highly sensitive to the orientation of porphyrin rings relative to each other [30–32]. Furthermore, it was previously established that the CD amplitude has a parabolic-like dependence on the dihedral angle between the coupling electronic transitions, with zero values at 0° and 180° and a maximum value at around 70° [81]. In the case of the porphyrin chromophores, there are two B electronic transitions orientated along the corresponding meso (5–15 and 10–20) positions (Figure 8B) and any directional deviation from the coplanar conformation makes these transitions optically active. In the crystal structure, both porphyrin planes are situated almost on the same line, with the dihedral angle Zn-C_{meso}-C_{meso}-Zn being 179.0°, which can be attributed to a slight anticlockwise orientation. In the structure optimized in dichloromethane, two porphyrin planes are orientated clockwise, with the dihedral angle Zn-C_{meso}-C_{meso}-Zn equaling −163.5°.

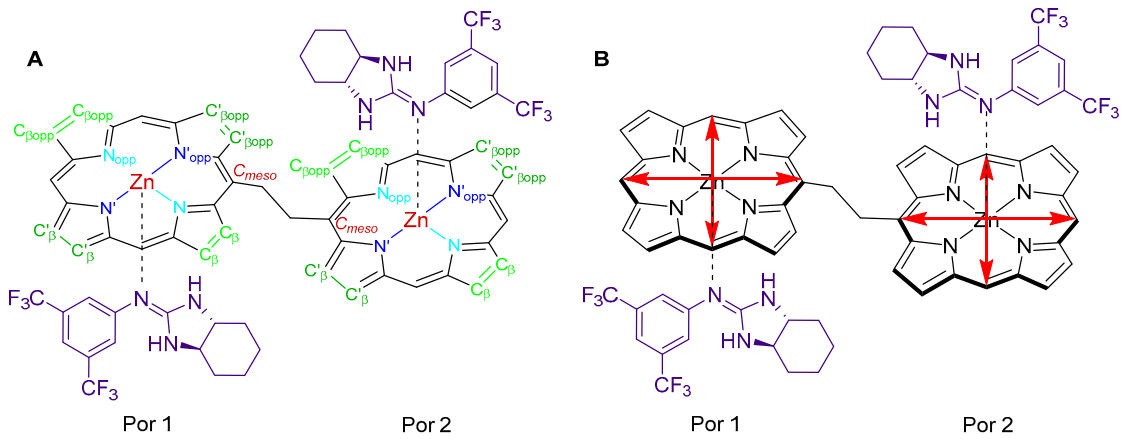

Figure 8. Atom labelling (**A**) and corresponding porphyrin electronic transitions (**B**) of the bis(ZnOEP)-BTI complex. Ethyl substituents in bis(ZnOEP) are omitted for clarity.

Table 1. Differences in the geometries in the solid-state (according to X-ray crystallography) and in the gas phase and solution (according to DFT calculations).

Angles	Experimental (Solid-State)	Fully Optimized (Gas)	Fully Optimized (CH_2Cl_2 Solution)
N-Zn-N_{opp} (Por 1)	160.6°	162.9°	160.8°
	161.2°	163.5°	161.0°
C_β-C_β-$C_{\beta opp}$-$C_{\beta opp}$ (Por 1)	9.4°	18.4°	18.1°
	−9.3°	−16.4°	−15.2°
N-Zn-N_{opp} (Por 2)	160.9°	164.0°	161.0°
	160.8°	163.5°	161.0°
C_β-C_β-$C_{\beta opp}$-$C_{\beta opp}$ (Por 2)	11.6°	10.9°	10.7°
	−13.5°	−11.7°	−11.9°
N_{guest}-Zn-N_{guest}-Zn	0.0°	6.4°	6.1°
Zn-C_{meso}-C_{meso}-Zn	179.0°	−162.2°	−163.5°

To confirm this hypothesis unambiguously, a relaxed coordinate scan along the Zn-C_{meso}-C_{meso}-Zn dihedral angle with the step of 2° using the RI-PB86-3D/def2-SV(P) level of theory and COSMO solvent model was carried out (corresponding energies are given in Table S4, see the Supplementary Materials). Further, for all these structures, the corresponding CD spectra using the ωB97X-D/cc-pVDZ level of theory with the SMD solvent model were simulated (corresponding data are given in Table S5, see the Supplementary Materials). The spectrum calculated was average weighted and based on the conformers' electronic energies (entropies and vibrational energies are not taken into account), as shown in Figure 9A. In this spectrum, the intensity of the 4th CE decreased by 63 cgs, and the intensities of the 3rd, 2nd, and 1st CEs increased by 158, 23, and 210 cgs, respectively, as

compared to the CD spectrum of complex A in solution. These values better match the experimental data; however, the intensities of the 2nd and 1st CEs are still relatively small (+265 and −335 cgs).

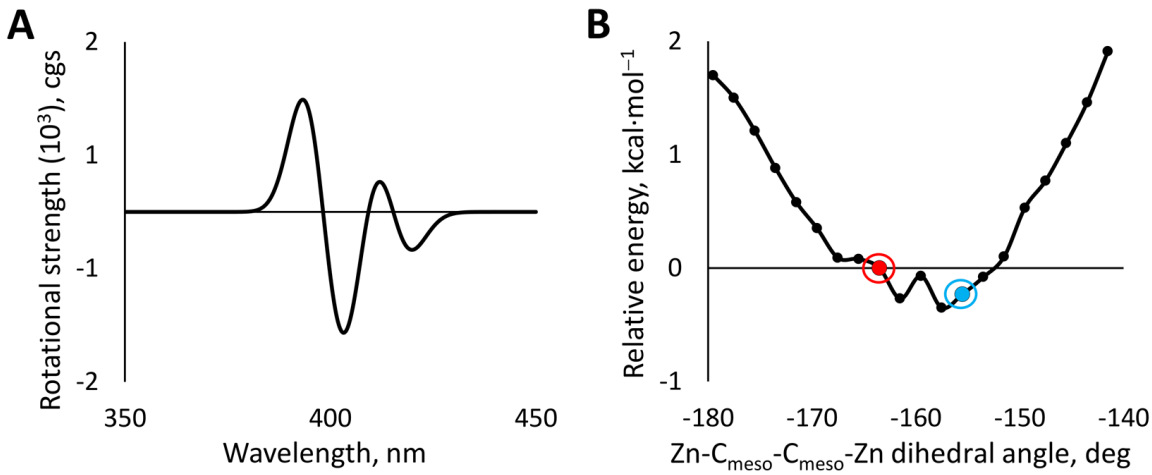

Figure 9. (**A**) Average simulated CD spectra, (**B**) the potential energy surface scan of the BTI/bis(ZnOEP) complex with variable Zn-C_{meso}-C_{meso}-Zn dihedral angles. Red marker shows the minimum found during the geometry optimization, blue marker shows the structure with the Zn-C_{meso}-C_{meso}-Zn dihedral angle of 155.5°.

In turn, the energy scan showed that the potential energy surface is flat and continues for the range of −167.5° to −151.5°, with the energies varying within just 0.4 kcal mol^{-1} (Figure 9B and Table S4, see the Supplementary Materials), which makes difficult to determine the exact minimum. Nevertheless, the minimum found by the geometry optimization process (and confirmed by frequency calculations) corresponds to the dihedral angle of −163.5° and it is 0.2 kcal mol^{-1} higher than in the case of the complex with the dihedral angle of −155.5°. Such a small energy difference is within an accuracy error of the DFT method and could be a result of the numerical noise. Therefore, it is plausible to assume that the Zn-C_{meso}-C_{meso}-Zn dihedral angle of bis(ZnOEP) complex in solution is about −155.5°, since the UV-Vis and CD spectra of this structure (Figure 10) has the best match with the experimentally measured spectrum (Figure 4). All other simulated spectra are presented in Figure S4, see the Supplementary Materials.

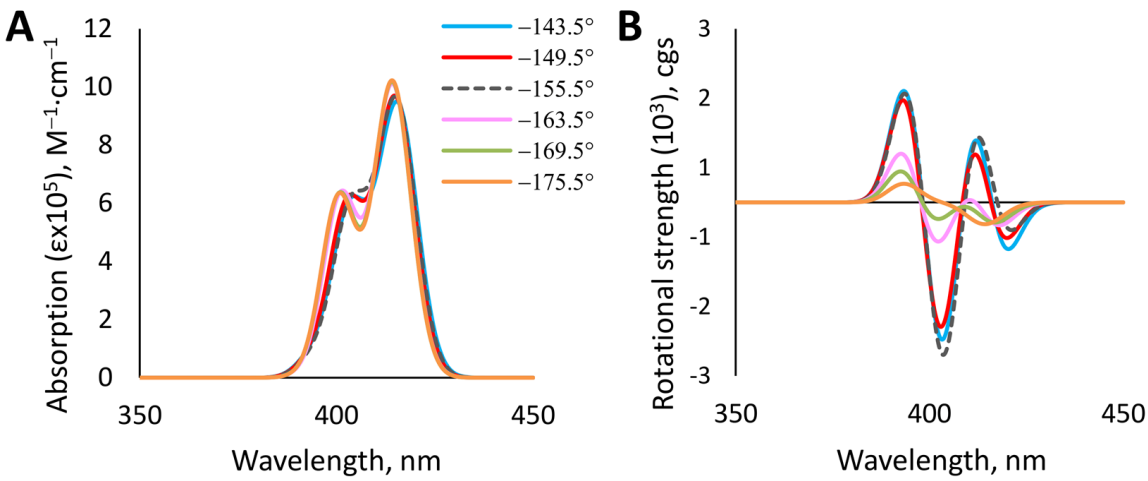

Figure 10. (**A**) Simulated UV-Vis spectra, (**B**) simulated CD spectra of bis(ZnOEP)/BTI complexes with variable Zn-C_{meso}-C_{meso}-Zn dihedral angles.

4. Conclusions

In the present work, the complexation of bis(trifluoromethyl)phenyl)octahydro-2H-benzo[d]imidazol-2-imine (BTI), as a guest, with bis(ZnOEP), as a host, was studied from the experimental and theoretical points of view. It was found that the host-guest complexation ratio is 1:2 and the BTI binding occurs via coordination of the imine group to the zinc ions of bis(ZnOEP). In agreement with the crystallographic results and DFT study, in solution the main host-guest complex is a supramolecule, in which the two guest molecules are located symmetrically at the opposite sides of bis(ZnOEP) host.

Complexation of the guests to bis(ZnOEP) causes the formation of a screw conformation in the bis-porphyrin host due to the shift of the porphyrin planes relative to each other, which results in low-energy shifts of the porphyrin electronic transitions and the appearance of a strong CD signal in the Soret band region. Although the simulated UV-Vis spectra based on solid-state geometry and structure optimized in the CH_2Cl_2 solution are similar, the CD spectra are more sensitive to geometry changes and differ drastically. The relative orientation of porphyrin planes changes upon solvation with the resultant complex, adopting a clockwise screw, with the Zn-C_{meso}-C_{meso}-Zn dihedral angle being *ca* $-155.5°$. The CD spectrum simulated for this spatial orientation is a good match with the experimental data and showed four clearly observed Cotton effects in the Soret band region induced by the chirogenic process of asymmetry transfer from a chiral guest to an achiral host.

This study is one of the rare examples of comprehensive CD analysis of chirality induction in bis-porphyrins caused by external chiral ligands, which can be a benchmark approach for the rationalization of supramolecular chirogenesis in bis-porphyrins. Furthermore, the obtained results demonstrate the necessity of careful consideration of all external and internal factors that influence the supramolecular organization of complex to attain the best match between experimental and simulated CD spectra.

Supplementary Materials: The following are available online at https://www.mdpi.com/2073-8994/13/2/275/s1, Figure S1: UV-Vis spectra of bis(ZnOEP) titration with BTI in CH_2Cl_2, Figure S2: UV-Vis experimental and 1:2 fitted titration curves of bis(ZnOEP) and BTI in CH_2Cl_2, Figure S3: Residual analysis of UV-Vis titration between bis(ZnOEP) and BTI in CH_2Cl_2 using 1:2 model, Figure S4: UV-vis and CD spectra simulated for complexes with altered Zn-C_{meso}-Zn-C_{meso} dihedral angle, Table S1: Absorptions of bis(ZnOEP) (3.3×10^{-6} M) derived from the UV-Vis titration of bis(ZnOEP) with BTI in CH_2Cl_2 and concentrations of BTI, Table S2: Transition energies, oscillator strengths and rotational strengths, Table S3: Energies of complexes A–F, Table S4: Energies of complexes optimized in CCl_2H_2 with frozen Zn-C_{meso}-C_{meso}-Zn dihedral angle, Table S5: Transition energies, oscillator strengths and rotational strengths for complexes with frozen Zn-C_{meso}-C_{meso}-Zn dihedral angle, Cartesian coordinates (Geometries.xyz).

Author Contributions: Computational studies, I.O. and E.C.; X-ray studies, K.-N.T. and K.R.; synthesis of BTI and spectroscopic host-guest binding studies, N.K.; conceptualization, D.K. and I.O.; methodology, I.O., E.C. and V.B.; formal analysis, I.O., K.-N.T. and N.K.; investigation, I.O. and N.K.; writing—original draft preparation, I.O.; writing—review and editing, D.K., V.B., K.-N.T., N.K. and R.A.; supervision, D.K., K.R., R.A. and E.C.; project administration, R.A.; funding acquisition, I.O., V.B. and R.A. All authors have read and agreed to the published version of the manuscript.

Funding: This work was supported by the Estonian Research Council grant PUTJD749 (for I.O.) PRG399, (for N.K., R.A., V.B.) and the European Union's H2020-FETOPEN grant 828779 (INITIO) (for N.K., K.-N.T., K.R., D.K., R.A., V.B.).

Institutional Review Board Statement: Not applicable.

Informed Consent Statement: Not applicable.

Data Availability Statement: Data presented in this study are available in the article and Supplementary Material.

Acknowledgments: Computations were performed on the HPC cluster at Tallinn University of Technology, which is part of the ETAIS project and partly on at Computational Chemistry laboratory

at Tallinn University of Technology, Estonia. I.O. acknowledges T. Tamm for his kind help. We also acknowledge T. Shalima (Tallinn University of Technology) for performing HRMS analysis.

Conflicts of Interest: The authors declare no conflict of interest.

References

1. Che, C.-M.; Lo, V.K.-Y.; Zhou, C.-Y.; Huang, J.-S. Selective functionalisation of saturated C–H bonds with metalloporphyrin catalysts. *Chem. Soc. Rev.* **2011**, *40*, 1950–1975. [CrossRef] [PubMed]
2. Barona-Castaño, J.C.; Carmona-Vargas, C.C.; Brocksom, T.J.; De Oliveira, K.T.; Graça, M.; Neves, P.M.S.; Amparo, M.; Faustino, F. Porphyrins as catalysts in scalable organic reactions. *Molecules* **2016**, *21*, 310. [CrossRef] [PubMed]
3. Meunier, B. Metalloporphyrins as versatile catalysts for oxidation reactions and oxidative DNA cleavage. *Chem. Rev.* **1992**, *92*, 1411–1456. [CrossRef]
4. Walter, M.G.; Rudine, A.B.; Wamser, C.C. Porphyrins and phthalocyanines in solar photovoltaic cells. *J. Porphyr. Phthalocyanines* **2010**, *14*, 759–792. [CrossRef]
5. Martínez-Díaz, M.V.; de la Torre, G.; Torres, T. Lighting porphyrins and phthalocyanines for molecular photovoltaics. *Chem. Commun.* **2010**, *46*, 7090–7108. [CrossRef] [PubMed]
6. Bottari, G.; Trukhina, O.; Ince, M.; Torres, T. Towards artificial photosynthesis: Supramolecular, donor–acceptor, porphyrin- and phthalocyanine/carbon nanostructure ensembles. *Coord. Chem. Rev.* **2012**, *256*, 2453–2477. [CrossRef]
7. Günsel, A.; Güzel, E.; Bilgiçli, A.T.; Şişman, İ.; Yarasir, M.N. Synthesis of non-peripheral thioanisole-substituted phthalocyanines: Photophysical, electrochemical, photovoltaic, and sensing properties. *J. Photochem. Photobiol. A Chem.* **2017**, *348*, 57–67. [CrossRef]
8. Xue, X.; Lindstrom, A.; Li, Y. Porphyrin-Based Nanomedicines for Cancer Treatment. *Bioconjug. Chem.* **2019**, *30*, 1585–1603. [CrossRef]
9. Cieplik, F.; Deng, D.; Crielaard, W.; Buchalla, W.; Hellwig, E.; Al-Ahmad, A.; Maisch, T. Antimicrobial photodynamic therapy—What we know and what we don't. *Crit. Rev. Microbiol.* **2018**, *44*, 571–589. [CrossRef]
10. Tsolekile, N.; Nelana, S.; Oluwafemi, O.S. Porphyrin as diagnostic and therapeutic agent. *Molecules* **2019**, *24*, 2669. [CrossRef]
11. Drain, C.M.; Varotto, A.; Radivojevic, I. Self-Organized Porphyrinic Materials. *Chem. Rev.* **2009**, *109*, 1630–1658. [CrossRef] [PubMed]
12. Borovkov, V. Effective Supramolecular Chirogenesis in Ethane-Bridged Bis-Porphyrinoids. *Symmetry* **2010**, *2*, 184–200. [CrossRef]
13. Borovkov, V. Supramolecular chirality in porphyrin chemistry. *Symmetry* **2014**, *6*, 256–294. [CrossRef]
14. Borovkov, V.; Inoue, Y. A Versatile Bisporphyrinoid Motif for Supramolecular Chirogenesis. *Eur. J. Org. Chem.* **2009**, *2*, 189–197. [CrossRef]
15. Chmielewski, P.J.; Siczek, M.; Stępień, M. Bis(N-Confused Porphyrin) as a Semirigid Receptor with a Chirality Memory: A Two-Way Host Enantiomerization through Point-to-Axial Chirality Transfer. *Chem. A Eur. J.* **2015**, *21*, 2547–2559. [CrossRef]
16. Paolesse, R.; Nardis, S.; Monti, D.; Stefanelli, M.; Di Natale, C. Porphyrinoids for Chemical Sensor Applications. *Chem. Rev.* **2017**, *117*, 2517–2583. [CrossRef]
17. Mathew, P.T.; Fang, F. Advances in Molecular Electronics: A Brief Review. *Engineering* **2018**, *4*, 760–771. [CrossRef]
18. Cook, L.; Brewer, G.; Wong-Ng, W. Structural aspects of porphyrins for functional materials applications. *Crystals* **2017**, *7*, 223. [CrossRef]
19. Chaudhri, N.; Sankar, M. Colorimetric "naked eye" detection of CN^-, F^-, CH_3COO^- and $H_2PO_4^-$ ions by highly nonplanar electron deficient perhaloporphyrins. *RSC Adv.* **2015**, *5*, 3269–3275. [CrossRef]
20. Hembury, G.A.; Borovkov, V.V.; Inoue, Y. Chirality-Sensing Supramolecular Systems. *Chem. Rev.* **2008**, *108*, 1–73. [CrossRef]
21. Ding, Y.; Zhu, W.-H.; Xie, Y. Development of Ion Chemosensors Based on Porphyrin Analogues. *Chem. Rev.* **2017**, *117*, 2203–2256. [CrossRef]
22. Carvalho, C.M.B.; Brocksom, T.J.; de Oliveira, K.T. Tetrabenzoporphyrins: Synthetic developments and applications. *Chem. Soc. Rev.* **2013**, *42*, 3302–3317. [CrossRef]
23. Geraci, G.; Parkhurst, L.J.B.T.-M. Circular dichroism spectra of hemoglobins. In *Methods in Enzymology*; Academic Press: Cambridge, MA, USA, 1981; Volume 76, pp. 262–275.
24. Ishiwari, F.; Fukasawa, K.; Sato, T.; Nakazono, K.; Koyama, Y.; Takata, T. A Rational Design for the Directed Helicity Change of Polyacetylene Using Dynamic Rotaxane Mobility by Means of Through-Space Chirality Transfer. *Chem. A Eur. J.* **2011**, *17*, 12067–12075. [CrossRef]
25. Balaz, M.; De Napoli, M.; Holmes, A.E.; Mammana, A.; Nakanishi, K.; Berova, N.; Purrello, R. A Cationic Zinc Porphyrin as a Chiroptical Probe for Z-DNA. *Angew. Chem.* **2005**, *117*, 4074–4077. [CrossRef]
26. Lu, H.; Kobayashi, N. Optically Active Porphyrin and Phthalocyanine Systems. *Chem. Rev.* **2016**, *116*, 6184–6261. [CrossRef]
27. Ito, S.; Hiroto, S.; Ousaka, N.; Yashima, E.; Shinokubo, H. Control of Conformation and Chirality of Nonplanar π-Conjugated Diporphyrins Using Substituents and Axial Ligands. *Chem. Asian J.* **2016**, *11*, 936–942. [CrossRef] [PubMed]
28. Huang, X.; Fujioka, N.; Pescitelli, G.; Koehn, F.E.; Williamson, R.T.; Nakanishi, K.; Berova, N. Absolute Configurational Assignments of Secondary Amines by CD-Sensitive Dimeric Zinc Porphyrin Host. *J. Am. Chem. Soc.* **2002**, *124*, 10320–10335. [CrossRef] [PubMed]
29. Borovkov, V.V.; Inoue, Y. Supramolecular Chirogenesis in Host-Guest Systems Containing Porphyrinoids. In *Supramolecular Chirality*; Crego-Calama, M., Reinhoudt, D.N., Eds.; Springer: Berlin/Heidelberg, Germany, 2006; Volume 625, pp. 89–146.

30. Borovkov, V.V.; Lintuluoto, J.M.; Inoue, Y. Supramolecular Chirogenesis in Bis(zinc porphyrin): An Absolute Configuration Probe Highly Sensitive to Guest Structure. *Org. Lett.* **2000**, *2*, 1565–1568. [CrossRef] [PubMed]
31. Borovkov, V.V.; Lintuluoto, J.M.; Inoue, Y. Supramolecular Chirogenesis in Zinc Porphyrins: Mechanism, Role of Guest Structure, and Application for the Absolute Configuration Determination. *J. Am. Chem. Soc.* **2001**, *123*, 2979–2989. [CrossRef]
32. Borovkov, V.V.; Lintuluoto, J.M.; Inoue, Y. Stoichiometry-Controlled Supramolecular Chirality Induction and Inversion in Bisporphyrin Systems. *Org. Lett.* **2002**, *4*, 169–171. [CrossRef] [PubMed]
33. Olsson, S.; Schäfer, C.; Blom, M.; Gogoll, A. Exciton-Coupled Circular Dichroism Characterization of Monotopically Binding Guests in Host−Guest Complexes with a Bis(zinc porphyrin) Tweezer. *ChemPlusChem* **2018**, *83*, 1169–1178. [CrossRef] [PubMed]
34. Takeda, S.; Hayashi, S.; Noji, M.; Takanami, T. Chiroptical Protocol for the Absolute Configurational Assignment of Alkyl-Substituted Epoxides Using Bis(zinc porphyrin) as a CD-Sensitive Bidentate Host. *J. Org. Chem.* **2019**, *84*, 645–652. [CrossRef] [PubMed]
35. Borovkov, V.V.; Fujii, I.; Muranaka, A.; Hembury, G.A.; Tanaka, T.; Ceulemans, A.; Kobayashi, N.; Inoue, Y. Rationalization of Supramolecular Chirality in a Bisporphyrin System. *Angew. Chem. Int. Ed.* **2004**, *43*, 5481–5485. [CrossRef] [PubMed]
36. Borovkov, V.V.; Lintuluoto, J.M.; Inoue, Y. Synthesis of Zn-, Mn, and Fe-containing mono- and heterometallated ethanediyl-bridged porphyrin dimers. *Helv. Chim. Acta* **1999**, *82*, 919–934. [CrossRef]
37. Dudziński, K.; Pakulska, A.M.; Kwiatkowski, P. An Efficient Organocatalytic Method for Highly Enantioselective Michael Addition of Malonates to Enones Catalyzed by Readily Accessible Primary Amine-Thiourea. *Org. Lett.* **2012**, *14*, 4222–4225. [CrossRef]
38. Cotton, F.A.; Murillo, C.A.; Wang, X.; Wilkinson, C.C. Strong reducing agents containing dimolybdenum Mo_2^{4+} units and their oxidized cations with $Mo_2^{5+/6+}$ cores stabilized by bicyclic guanidinate anions with a seven-membered ring. *Dalton Trans.* **2006**, *38*, 4623–4631. [CrossRef]
39. Online Tools for Supramolecular Chemistry Research and Analysis. Available online: http://supramolecular.org/ (accessed on 7 January 2021).
40. Hirose, K. A Practical Guide for the Determination of Binding Constants. *J. Incl. Phenom.* **2001**, *39*, 193–209. [CrossRef]
41. Hibbert, D.B.; Thordarson, P. The death of the Job plot, transparency, open science and online tools, uncertainty estimation methods and other developments in supramolecular chemistry data analysis. *Chem. Commun.* **2016**, *52*, 12792–12805. [CrossRef]
42. Rigaku Oxford Diffraction. *CrysAlisPro Software System, Version 38.46*; Rigaku Corporation: Oxford, UK, 2017.
43. Sheldrick, G.M. A short history of *SHELX*. *Acta Cryst.* **2008**, *A64*, 112–122. [CrossRef]
44. Sheldrick, G.M. *SHELXL13. Program Package for Crystal Structure Determination from Single Crystal Diffraction Data*; University of Göttingen: Göttingen, Germany, 2013.
45. Sheldrick, G.M. Crystal structure refinement with SHELXL. *Acta Cryst.* **2015**, *C71*, 3–8.
46. Hirshfeld, F.L. Can X-ray data distinguish bonding effects from vibrational smearing? *Acta Cryst.* **1976**, *A32*, 239–244. [CrossRef]
47. Thorn, A.; Dittrich, B.; Sheldrick, G.M. Enhanced rigid-bond restraints. *Acta Cryst.* **2012**, *A68*, 448–451. [CrossRef]
48. Eichkorn, K.; Treutler, O.; Öhm, H.; Häser, M.; Ahlrichs, R. Auxiliary basis sets to approximate Coulomb potentials. *Chem. Phys. Lett.* **1995**, *240*, 283–290. [CrossRef]
49. Eichkorn, K.; Weigend, F.; Treutler, O.; Ahlrichs, R. Auxiliary basis sets for main row atoms and transition metals and their use to approximate Coulomb potentials. *Theor. Chem. Acc.* **1997**, *97*, 119–124. [CrossRef]
50. Sierka, M.; Hogekamp, A.; Ahlrichs, R. Fast evaluation of the Coulomb potential for electron densities using multipole accelerated resolution of identity approximation. *J. Chem. Phys.* **2003**, *118*, 9136–9148. [CrossRef]
51. Becke, A.D. Density-functional exchange-energy approximation with correct asymptotic behavior. *Phys. Rev. A* **1988**, *38*, 3098–3100. [CrossRef]
52. Perdew, J.P. Density-functional approximation for the correlation energy of the inhomogeneous electron gas. *Phys. Rev. B* **1986**, *33*, 8822–8824. [CrossRef]
53. Grimme, S.; Antony, J.; Ehrlich, S.; Krieg, H. A consistent and accurate ab initio parametrization of density functional dispersion correction (DFT-D) for the 94 elements H-Pu. *J. Chem. Phys.* **2010**, *132*, 154104. [CrossRef] [PubMed]
54. Schäfer, A.; Horn, H.; Ahlrichs, R. Fully optimized contracted Gaussian basis sets for atoms Li to Kr. *J. Chem. Phys.* **1992**, *97*, 2571–2577. [CrossRef]
55. TURBOMOLE V7.0 2015, A Development of University of Karlsruhe and Forschungszentrum Karlsruhe GmbH, 1989–2007, TURBOMOLE GmbH, Since 2007. Available online: http://www.turbomole.com (accessed on 7 January 2021).
56. Martynov, A.G.; Mack, J.; May, A.K.; Nyokong, T.; Gorbunova, Y.G.; Tsivadze, A.Y. Methodological Survey of Simplified TD-DFT Methods for Fast and Accurate Interpretation of UV–Vis–NIR Spectra of Phthalocyanines. *ACS Omega* **2019**, *4*, 7265–7284. [CrossRef] [PubMed]
57. Osadchuk, I.; Borovkov, V.; Aav, R.; Clot, E. Benchmarking computational methods and influence of guest conformation on chirogenesis in zinc porphyrin complexes. *Phys. Chem. Chem. Phys.* **2020**, *22*, 11025–11037. [CrossRef]
58. Conradie, J.; Ghosh, A. Energetics of Saddling versus Ruffling in Metalloporphyrins: Unusual Ruffled Dodecasubstituted Porphyrins. *ACS Omega* **2017**, *2*, 6708–6714. [CrossRef]
59. Andzelm, J.; Kölmel, C.; Klamt, A. Incorporation of solvent effects into density functional calculations of molecular energies and geometries. *J. Chem. Phys.* **1995**, *103*, 9312–9320. [CrossRef]
60. Weigend, F. Accurate Coulomb-fitting basis sets for H to Rn. *Phys. Chem. Chem. Phys.* **2006**, *8*, 1057–1065. [CrossRef] [PubMed]

61. Frisch, M.J.; Trucks, G.W.; Schlegel, H.B.; Scuseria, G.E.; Robb, M.A.; Cheeseman, J.R.; Scalmani, G.; Barone, V.; Petersson, G.A.; Nakatsuji, H.; et al. *Gaussian 16, Revision A.03*; Gaussian, Inc.: Wallingford, CT, USA, 2016.
62. Bauernschmitt, R.; Ahlrichs, R. Treatment of electronic excitations within the adiabatic approximation of time dependent density functional theory. *Chem. Phys. Lett.* **1996**, *256*, 454–464. [CrossRef]
63. Stratmann, R.E.; Scuseria, G.E.; Frisch, M.J. An efficient implementation of time-dependent density-functional theory for the calculation of excitation energies of large molecules. *J. Chem. Phys.* **1998**, *109*, 8218–8224. [CrossRef]
64. Casida, M.E.; Jamorski, C.; Casida, K.C.; Salahub, D.R. Molecular excitation energies to high-lying bound states from time-dependent density-functional response theory: Characterization and correction of the time-dependent local density approximation ionization threshold. *J. Chem. Phys.* **1998**, *108*, 4439–4449. [CrossRef]
65. Chai, J.-D.; Head-Gordon, M. Long-range corrected hybrid density functionals with damped atom–atom dispersion corrections. *Phys. Chem. Chem. Phys.* **2008**, *10*, 6615–6620. [CrossRef]
66. Dunning, T.H. Gaussian basis sets for use in correlated molecular calculations. I. The atoms boron through neon and hydrogen. *J. Chem. Phys.* **1989**, *90*, 1007–1023. [CrossRef]
67. Woon, D.E.; Dunning, T.H. Gaussian basis sets for use in correlated molecular calculations. III. The atoms aluminum through argon. *J. Chem. Phys.* **1993**, *98*, 1358–1371. [CrossRef]
68. Peterson, K.A.; Woon, D.E.; Dunning, T.H. Benchmark calculations with correlated molecular wave functions. IV. The classical barrier height of the $H+H_2 \rightarrow H_2+H$ reaction. *J. Chem. Phys.* **1994**, *100*, 7410–7415. [CrossRef]
69. Marenich, A.V.; Cramer, C.J.; Truhlar, D.G. Universal Solvation Model Based on Solute Electron Density and on a Continuum Model of the Solvent Defined by the Bulk Dielectric Constant and Atomic Surface Tensions. *J. Phys. Chem. B* **2009**, *113*, 6378–6396. [CrossRef] [PubMed]
70. Konrad, N.; Meniailava, D.; Osadchuk, I.; Adamson, J.; Hasan, M.; Clot, E.; Aav, R.; Borovkov, V.; Kananovich, D. Supramolecular chirogenesis in zinc porphyrins: Complexation with enantiopure thiourea derivatives, binding studies and chirality transfer mechanism. *J. Porphyr. Phthalocyanines* **2019**, *24*, 840–849. [CrossRef]
71. Dennington, R.; Keith, T.A.; Millam, J.M. *GaussView, Version 6*; Semichem Inc.: Shawnee Mission, KS, USA, 2016.
72. Borovkov, V.V.; Lintuluoto, J.M.; Inoue, Y. Syn-Anti Conformational Changes in Zinc Porphyrin Dimers Induced by Temperature-Controlled Alcohol Ligation. *J. Phys. Chem. B* **1999**, *24*, 5151–5156. [CrossRef]
73. Borovkov, V.V.; Lintuluoto, J.M.; Sugeta, H.; Fujiki, M.; Arakawa, R.; Inoue, Y. Supramolecular Chirogenesis in Zinc Porphyrins: Equilibria, Binding Properties, and Thermodynamics. *J. Am. Chem. Soc.* **2002**, *124*, 2993–3006. [CrossRef] [PubMed]
74. Sahoo, D.; Guchhait, T.; Rath, S.P. Spin Modulation in Highly Distorted Fe^{III} Porphyrinates by Using Axial Coordination and Their π-Cation Radicals. *Eur. J. Inorg. Chem.* **2016**, *21*, 3441–3453. [CrossRef]
75. Zhang, J.; Tang, M.; Chen, D.; Lin, B.; Zhou, Z.; Liu, Q. Horizontal and Vertical Push Effects in Saddled Zinc Porphyrin Complexes: Implications for Heme Distortion. *Inorg. Chem.* **2019**, *58*, 2627–2636. [CrossRef]
76. Guberman-Pfeffer, M.J.; Greco, J.A.; Samankumara, L.P.; Zeller, M.; Birge, R.R.; Gascón, J.A.; Brückner, C. Bacteriochlorins with a Twist: Discovery of a Unique Mechanism to Red-Shift the Optical Spectra of Bacteriochlorins. *J. Am. Chem. Soc.* **2017**, *139*, 548–560. [CrossRef]
77. Hajizadeh, F.; Reisi-Vanani, A.; Azar, Y.T. Theoretical design of Zn-dithiaporphyrins as sensitizer for dye-sensitized solar cells. *Curr. Appl. Phys.* **2018**, *18*, 1122–1133. [CrossRef]
78. Sánchez-Bojorge, N.A.; Zaragoza-Galán, G.; Flores-Holguín, N.R.; Chávez-Rojo, M.A.; Castro-García, C.; Rodríguez-Valdez, L.M. Theoretical analysis of the electronic properties in Zinc-porphyrins derivatives. *J. Mol. Struct.* **2019**, *1191*, 259–270. [CrossRef]
79. Thomassen, I.K.; Vazquez-Lima, H.; Gagnon, K.J.; Ghosh, A. Octaiodoporphyrin. *Inorg. Chem.* **2015**, *54*, 11493–11497. [CrossRef] [PubMed]
80. Farley, C.; Bhupathiraju, N.V.S.D.K.; John, B.K.; Drain, C.M. Tuning the Structure and Photophysics of a Fluorous Phthalocyanine Platform. *J. Phys. Chem. A* **2016**, *120*, 7451–7746. [CrossRef] [PubMed]
81. Harada, N.; Nakanishi, K. *Circular Dichroic Spectroscopy. Exciton Coupling in Organic Stereochemistry*; University Science Books: Mill Valley, CA, USA, 1983; pp. 1–406.